Accepted Manuscript

Metal-organic framework-derived Co_3O_4 covered by MoS_2 nanosheets for high-performance lithium-ion batteries

Jinpei Wang, Hu Zhou, Meizhou Zhu, Aihua Yuan, Xiaoping Shen

PII: S0925-8388(18)30527-9

DOI: 10.1016/j.jallcom.2018.02.086

Reference: JALCOM 44962

To appear in: *Journal of Alloys and Compounds*

Received Date: 26 October 2017

Revised Date: 26 January 2018

Accepted Date: 8 February 2018

Please cite this article as: J. Wang, H. Zhou, M. Zhu, A. Yuan, X. Shen, Metal-organic framework-derived Co_3O_4 covered by MoS_2 nanosheets for high-performance lithium-ion batteries, *Journal of Alloys and Compounds* (2018), doi: 10.1016/j.jallcom.2018.02.086.

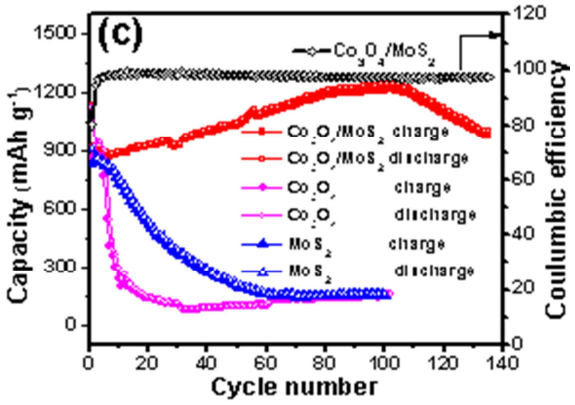

Metal-organic framework-derived Co_3O_4 covered by MoS_2 nanosheets for high-performance lithium-ion batteries

Jinpei Wang [a], Hu Zhou [b,*], Meizhou Zhu [b], Aihua Yuan [a,c*], Xiaoping Shen [d]

[a]*School of Environmental and Chemical Engineering,* [b]*School of Material Science and Engineering, and* [c]*Marine Equipment and Technology Institute, Jiangsu University of Science and Technology, Zhenjiang 212003, P. R. China*

[d]*School of Chemistry and Chemical Engineering, Jiangsu University, Zhenjiang 212013, P. R. China*

* Corresponding authors. Tel.: +86 511 85639001.

E-mail address: aihua.yuan@just.edu.cn (A.H. Yuan); zhmiao119@sina.com (H. Zhou).

Abstract: MOF-derived Co_3O_4 covered by MoS_2 nanosheets was synthesized and applied in the field of lithium-ion batteries. The discharge capacity of Co_3O_4/MoS_2 reached 1200.0 mAh g^{-1} after 100 cycles at the current density of 100 mA g^{-1}, much higher than those of pure Co_3O_4 and MoS_2. Moreover, the capacities of Co_3O_4/MoS_2 varied from 903.7 to 397.9 mAh g^{-1} upon increasing the current densities from 100 to 800 mA g^{-1}. The remarkable performance was attributed to the unique composite structure, in which the inner Co_3O_4 particles can store lithium ions and act as the transportation medium of electrons, enabling outstanding charge/discharge abilities of MoS_2, while the outer MoS_2 nanosheets can release the bulk volume expansion of metal oxides during the charge/discharge reactions.

Keywords: Lithium-ion battery; Molybdenum disulfide; Metal-organic frameworks; Metal oxides; Anode material

1. Introduction

Nowadays, the global energy crisis and requirement for environmental protection are attracting great attention on energy storage and energy conversion systems such as electrochemical energy storage, hydrogen storage, etc [1-4]. Lithium-ion batteries (LIBs) with high capacities have been extensively applied for wearable electronic equipments and electric vehicle for energy storage because of their merits such as no memory effect and environment-benevolent. The electrode materials are the primary components of LIBs. However, the research for new types of electrode materials with greater specific surface areas, higher storage capacities of Li^+ ions, and shorter ion and electron transport paths still remains a huge challenge [5, 6].

With the unique structural features and facile synthesis procedures, metal-organic frameworks (MOFs) have been utilized as templates and/or precursors to obtain porous metal oxides or carbon for the application in energy storage and conversion [7-13]. Considerable work have demonstrated that MOFs can be easily transformed to porous metal oxides through the simple high-temperature calcinations, and the obtained metal oxides preserve the features of MOFs precursors such as large surface areas, suitable voids and tunable architectures [8, 9]. Among these metal oxides applied in anode materials, Co_3O_4 is expected to meet the requirements for LIBs in the future because of its high theoretical capacity of 890 mAh g^{-1} [14, 15]. Unfortunately, similar to other metal oxides, Co_3O_4 usually suffers from poor capacity retention and/or rate capabilities during the cycling process. It mainly results from the low electrical transportation and dramatic volume variations, as well as the side reactions reacting at the electrode-electrolyte interface [5, 16]. Hence, a growing interest in surface coating has been shown in solving the above disadvantages. To solve the above problem, a large number of Co_3O_4-based composites have been dedicated to electrode materials so far, which are decorated by metal oxides, carbonaceous materials or other materials such as Co_3O_4/TiO_2, graphene/Co_3O_4, CNT/Co_3O_4, [17-21] etc. These

composites not only prevent the aggregation of Co_3O_4, but also efficiently accommodate the volume variation of Co_3O_4 by providing flexible cushion space. It is still a hard task for business applications, although considerable improved performances have been demonstrated.

Among the various commercial anode materials of LIBs, graphite is widely employed. However, this material possesses a relatively low theoretical capacity (372 mAh g^{-1}). So it is unable to meet the requirement for massive batteries of high-energy density. Compared with conditional graphite, transition-metal sulfides (MoS_2, WS_2, ReS_2) have exhibited higher capacities than the intercalation-based graphite anodes. In addition, similar to graphite, MoS_2 has a two dimensional (2D) layered structure. The spacing of adjacent layers is connected by the weak Vander Waals, which will promote the ions insertion and extraction process during the charge/discharge cycling [22-24]. And yet, MoS_2 has a poor cycling performance because of the substantial volumetric change. Meanwhile, a rapid capacity decline at high charge/discharge current density results from semiconducting property of MoS_2 [25-31]. Therefore, MoS_2 with different morphologies via structure modification have been reported for energy usage [25, 26]. In addition, high-performance MoS_2-based composites have also been constructed for energy application with a handy and commercial method. Su et al. synthesized nano-TiO_2-decorated MoS_2 nanosheets for LIBs which delivered a high capacity [29]. Chen et al. constructed a nanocomposite MoS_2/Co_3O_4 with an excellent electrochemical performance [30]. In the meantime, MoS_2 nanosheets-covered structures have been prepared for energy storage, catalysis and other applications [32-34]. In fact, it should be noted that very little optimization work has been done on the composites of MOFs and MoS_2 for practical applications (Table S1). Zheng et al. prepared the MNCD@MoS_2 composite (MNCD: microporous nitrogen-doped carbon dodecahedron) by employing ZIF-8 as precursor, and the electrode exhibited ultrafast and stable charge/discharge abilities for LIBs [35].

The current work show that the composites from MoS_2 and Co_3O_4 display excellent performances for energy storage. Based on these studies, our work

extends the knowledge to a facile method to prepare MOF-derived Co_3O_4/MoS_2 composite, as shown in Scheme 1. The Co-based MOF, ZIF-67, was firstly prepared and then the as-prepared ZIF-67 particles were thermally treated to obtain high-symmetric Co_3O_4 dodecahedrons. Finally, the Co_3O_4/MoS_2 composite was constructed by a hydrothermal synthesis process. The lithium storage performance of Co_3O_4/MoS_2 was discussed in detail. The results show that the composite electrode displays a high rechargeable capacity of ~1200 mAh g^{-1} after 100 cycles at a current rate of 100 mA g^{-1}, and exhibits an improved cycling stability than pure Co_3O_4 and MoS_2. The excellent electrochemical performances result from the designed unique structure composing of inner Co_3O_4 particles and outer MoS_2 nanosheets, which maximally take advantages of electrochemical activities of both components. Moreover, the outer MoS_2 nanosheets can effectively accommodate large volumetric expansion of inner Co_3O_4 particles. In addition, the Co_3O_4 component provides a fast path for electron transportation. As far as we know, there are only two samples of MOF-derived metal oxide/MoS_2 composites. Zang et al. synthesized crystalline MoS_2@TiO_2 to promote catalytic activity for hydrogen evolution reaction (HER) [36]. Yin et al. demonstrated a facile two-step hydrothermal method to synthesize MoS_2 coupled MOF-derived TiO_2 for photoelectrochemical water splitting and dye sensitized solar cells [37]. Our work is the first example of MOF-derived metal oxide composited with MoS_2 for the application in energy storage.

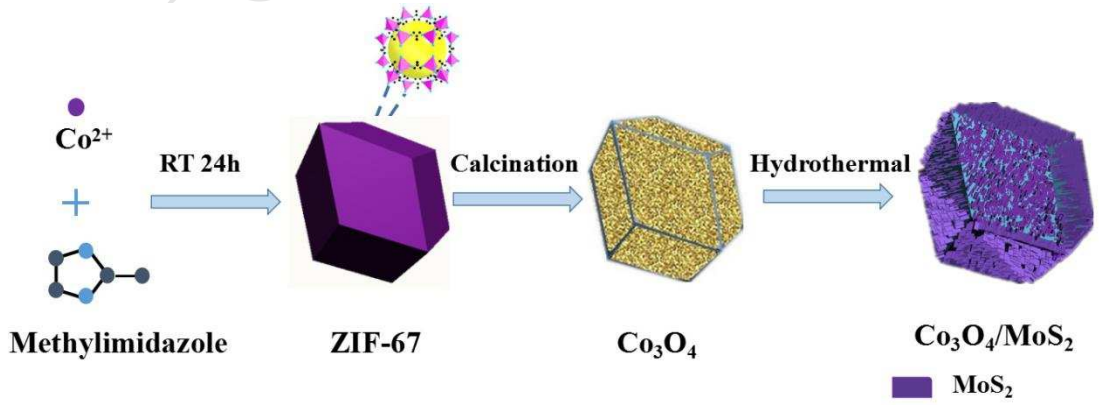

Scheme 1 Formation process of the Co_3O_4/MoS_2 composite.

2. Experimental details

2.1. Chemical reagents

Cobalt nitrate hexahydrate ($Co(NO_3)_2 \cdot 6H_2O$), 2-methylimidazole, thiourea and ammonium molybdate tetrahydrate ($(NH_4)_6Mo_7O_{24} \cdot 4H_2O$) were supplied from Energy Chemical. All chemicals were used without further purification.

2.2. Synthesis of ZIF-67

ZIF-67 was prepared according to the reported method [38, 39]. 1.455 g $Co(NO_3)_2 \cdot 6H_2O$ was dissolved in a methanolic solution (MeOH) to form solution **A**, while 1.642 g 2-methylimidazole was dissolved in another 40 mL MeOH to give solution **B**. After that, solution **A** was slowly dripped into solution **B** and then magnetically stirred vigorously for 30 seconds. The mixed solution was aged under room temperature without any intervention for 24 h. The purple ZIF-67 precipitates were separated from the solution by centrifugation, following by washing thoroughly many times with methanol and absolute ethanol. The products were finally dried at 60 °C for 12 h under vacuum condition.

2.3. Synthesis of Co_3O_4

Co_3O_4 was prepared through the calcination of ZIF-67 precursor. In brief, the products of ZIF-67 were placed in a furnace. Then the temperature was heated to 350 °C at a rate of 1 °C min^{-1} and kept at this temperature for 30 min in nitrogen atmosphere. After that, the nitrogen gas was turned off and the stove was kept at the temperature constantly under air gas flow for further 60 min. After cooling to room temperature naturally, the resultant black Co_3O_4 particles were obtained.

2.4. Synthesis of Co_3O_4/MoS_2

Co_3O_4/MoS_2 was synthesized by a one-step hydrothermal reaction, using ammonium molybdate tetrahydrate, thiourea and as-prepared Co_3O_4 as starting materials. 80 mg Co_3O_4 products were added into 40 mL deonized water by ultrasound for 30 min. Then, 0.35 g (0.28 mmol) ammonium molybdate tetrahydrate and 0.76 g (10 mmol) thiourea were dissolved into the solution.

After ultrasonic treatment, the solution became homogeneous. Being stirred for 1 h, the composite was synthesized by hydrothermal treatment of the precursor solution in a dried Teflon-lined stainless steel autoclave with 60% of the total volume. And then, the autoclave was treated at 200 °C for 15 h. Once being cooled down naturally, the resulting Co_3O_4/MoS_2 precipitates were collected by centrifugation, washed with de-ionized water and ethanol for several times. And then, the collected precipitates were dried at 60 °C in vacuum overnight. For comparison, two Co_3O_4/MoS_2 composites with different mass ratios of MoS_2:Co_3O_4 were prepared by varying the mass (20 mg, 130 mg) of Co_3O_4 components during the synthesis process of composites. The as-obtained materials were named as L-Co_3O_4/MoS_2 and H-Co_3O_4/MoS_2, respectively. Furthermore, pure MoS_2 was also prepared as above method in the absence of Co_3O_4.

2.5. Characterization

X-ray powder diffraction (XRD) patterns were recorded on a Shimadzu XRD-6000 X-ray diffractometer with Cu K_α (λ =0.15406) to evaluate the crystal structure of the as-synthesized samples. X-ray photoelectron spectroscopy (XPS, Thermo Fisher Scientific ESCALAB 250) using Al-K_α radiation with a base pressure of 5×10^{-10} mbar was employed to analyze the surface species and nature of elements present in the heterostructure. The morphology and structural characterization of the samples were carried out by transmission electron microscopy (TEM, JOEL JEM2100F), scanning electron microscopy (FE-SEM, ZEISS Merlin Compact). Energy dispersive spectroscopic (EDS) were characterized by Oxford X-Max.

2.6. Electrochemical measurements

The electrochemical measurements of as-prepared materials were done using standard 2032-type coin cells. The CR2032 type lithium coin cells were assembled inside a glove box (LABSTAR-M Braun) filled with ultra-high pure argon maintained (O_2 and H_2O levels < 0.5 ppm). Celgard 2600 was used as the separator and metallic lithium foil was applied as the counter and reference electrode. The electrolyte was 1 M $LiPF_6$ with the mixed solution of ethylene carbonate and diethyl carbonate (1:1 by

volume). The working electrode materials were prepared with 75 wt% of active materials (Co_3O_4, MoS_2 or Co_3O_4/MoS_2), 15 wt% of Super P block carbon and 10 wt% of binder polyvinylidene fiuoride (PVDF) in N-methyl-2-pyrrolidone (NMP) solution to form homogeneous slurries. Subsequently, the well-mixed slurry was uniformly tape-casted onto copper foil and dried to remove the solvent at 80 ^oC for 12 h under a vacuum condition. Galvanostatic charge-discharge measurements and rate-performance tests under different current densities were carried out in a LAND CT 2001A (Wuhan Rambo Testing Equipment Co. Ltd) between 0.01 and 3.0 V. Cyclic voltammetry (CV) behaviors and electrochemical impedance spectroscopy (EIS) performances of all samples were studied with a CHI660D electrochemical work station (Chenhua, Shanghai, China) using a standard three-electrode setup. The CV curves were conducted in the voltage range of 0.01-3 V vs. Li/Li^+ with a scan rate of 0.2 mV s^{-1}. EIS tests were performed over the frequency range from 0.01 Hz to 100 kHz by applying a sine wave with amplitude of 5 mV at room temperatures.

3. Results and discussion

3.1. Powder X-ray diffraction

All X-ray diffraction peaks of as-prepared Co_3O_4 and MoS_2 can be indexed well with the Co_3O_4 (JCPDS card no. 42-1467) and hexagonal MoS_2 (JCPDS card no. 37-1492), respectively (Fig. S1). The diffraction peak at 14.2° in XRD patterns of the composite (Fig. 1) corresponds to the (002) plane of the hexagonal 2H-MoS_2, which accounts to the typical interlayer distance of 0.63 nm in the following high resolution (HR) TEM image. This peak reveals a well-stacked layered structure of MoS_2. The (002) plane for pure MoS_2 (Fig. S1) moves slightly toward small angle because of the formation of chaotic layers, which results in lattice defects or strain generation. The diffraction peaks at 2θ = 32.6° can be assigned to (100) plane, and 2θ = 58.2° can be indexed to (110) plane of 2H-MoS_2, respectively [40, 41]. Both peaks could be obviously observed in XRD patterns of the composite (Fig. 1).

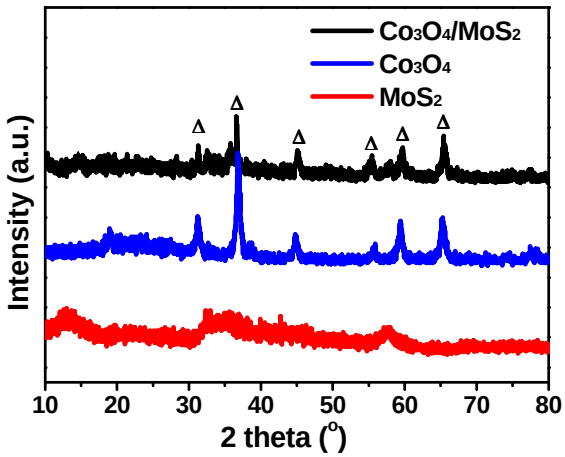

Fig. 1 Powder XRD patterns of MoS_2, Co_3O_4, and Co_3O_4/MoS_2 (□ and △symbols represent characteristic diffraction peaks of MoS_2 and Co_3O_4, respectively)

3.2. X-ray photoelectron spectroscopy

The XPS survey spectrum of Co_3O_4/MoS_2 (Fig. S2) manifested the presence of molybdenum, sulfur, cobalt, and oxygen elements. As for the Co component, the Co 2p spectrum is shown in Fig. 2a, which displays a doublet at binding energies of about 779.3 and 794.4 eV, corresponding to Co $2p_{3/2}$ and Co $2p_{1/2}$ spin orbit coupling levels, respectively [16, 42]. Fig. 2b shows the O 1s binding energies. The peak at 530.1 eV in the XPS spectrum of O 1s core level for Co_3O_4/MoS_2 can be assigned to the surface lattice O^{2-} of metal oxides. Besides, the peak at 531.6 eV corresponds to the adsorbed oxygen and hydroxyl group [42]. This result confirms that Co_3O_4 is the main cobalt phase in the composite. The composite is proved to undoubtedly contain 2H-phase MoS_2 with the Mo $3d_{5/2}$, Mo $3d_{3/2}$, S $2p_{3/2}$, and S $2p_{1/2}$ orbital spins. Figure 2c shows the high-resolution XPS spectrum of Mo 3d core levels for the composite. Two peaks at 228.9 and 232.1 eV correspond to the binding energies of Mo $3d_{5/2}$ and Mo $3d_{3/2}$, respectively. These two peaks are characteristic values for Mo^{4+} in MoS_2 and very close to those reported in literatures [35, 41]. Moreover, a small and slightly lower binding energy (~226 eV) than that for Mo $3d_{5/2}$ can be observed, which is the specific value for S 2s. In XPS spectrum of S 2p (Fig. 2d), two peaks at 162.1 and 163.2 eV can be consistent with S $2p_{3/2}$ and S $2p_{1/2}$, respectively, indicating the existence of S^{2-} [35, 41]. The survey and narrow scans demonstrate that Co_3O_4/MoS_2 is free of other impurities and the Mo and S elements are present as the MoS_2 phase.

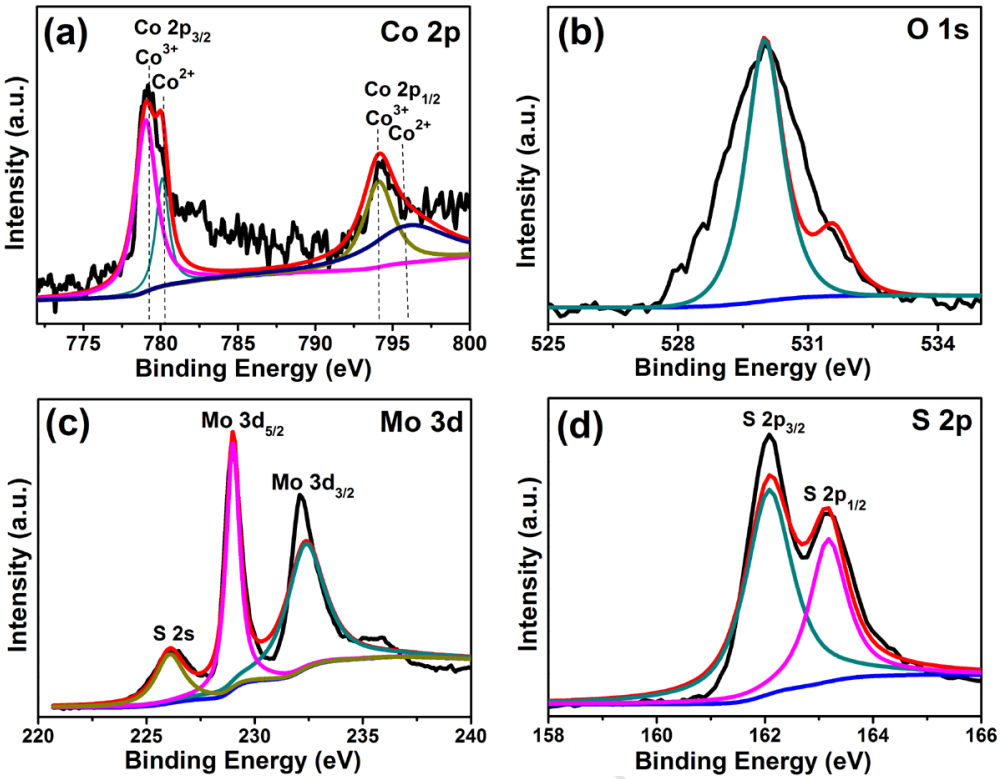

Fig. 2 XPS spectra of Co_3O_4/MoS_2: (a) Co 2p, (b) O 1s, (c) Mo 3d, and (d) S 2p.

3.3. Morphologies

The morphologies and structures of as-prepared ZIF-67, Co_3O_4, MoS_2 and Co_3O_4/MoS_2 were examined by SEM and TEM, as shown in Fig. 3. The SEM image (Fig. 3a) reveals that these rhombic dodecahedrons have smooth surfaces and sharp edges. Fig. 3b shows that the Co_3O_4 products preserve the features of MOF precursors with the uniform size and rhombic dodecahedral morphology. It has to be mentioned that the surface of Co_3O_4 is rougher than ZIF-67. Actually, the organic linker in the structure of MOF can efficiently prevent the aggregation of the resulting nanometer particles in the primary MOF, generating numerous voids in the final metal oixdes with rough surface. SEM image of Co_3O_4 reveals that the particles have uniform dodecahedrons with the average size of about 600 nm. The pure MoS_2 has a structure of aggregated flower-like microspheres, which are made up from interconnected nanosheets with the nanometer-scale thinness (Fig. 3c). In comparison, the Co_3O_4/MoS_2 composite was prepared through the hydrothermal synthetic growth of MoS_2 on Co_3O_4 particles (Fig. 3d). In more detail, the enlarged SEM image indicates that MoS_2 nanosheets are grown on the rough surface of Co_3O_4 after the hydrothermal

reaction. The internal structure of Co_3O_4/MoS_2 is further investigated by employing TEM. As can be seen from Fig. 3e, the surfaces of Co_3O_4 particles are covered by numerous MoS_2 nanosheets, in sharp contrast to the surface of pure Co_3O_4. A clear structure of the Co_3O_4/MoS_2 composite which MoS_2 nanosheets are grown on Co_3O_4 dodecahedrons can be seen from Fig. 3f. The successful preparation of Co_3O_4/MoS_2 validates that the Co_3O_4 dodecahedron can serve as a good template for the deposition of MoS_2. The growth mechanism of the composites can be described as follows. MoS_2 nanosheets are produced through a hydrothermal reaction between ammonium molybdate tetrahydrate and thiourea, and simultaneously uniformly dispersed on the surface of Co_3O_4 particles derived from ZIF-67 [43]. EDS mapping analysis (Fig. 3g) reveals that the successful decoration of Co_3O_4 particles with MoS_2 nanosheets, due to the uniform distribution of four elements (Co, Mo, O and S) in the whole area. HRTEM image of Fig. 3h shows clear fringes with an interlayer distance of ca. 0.63 nm for the (002) basal planes of the hexagonal MoS_2 structure. The fringes with a lattice spacing of 0.23 nm and 0.46 nm can be indexed to the (222) and (111) planes of the dodecahedron Co_3O_4, respectively [30, 39]. Furthermore, the selected area electron diffraction (SAED) pattern is shown in the inset picture of Fig. 3h. The diffraction rings correspond well with the (002), (100) planes of MoS_2, (111), (400) and (222) planes of Co_3O_4, respectively.

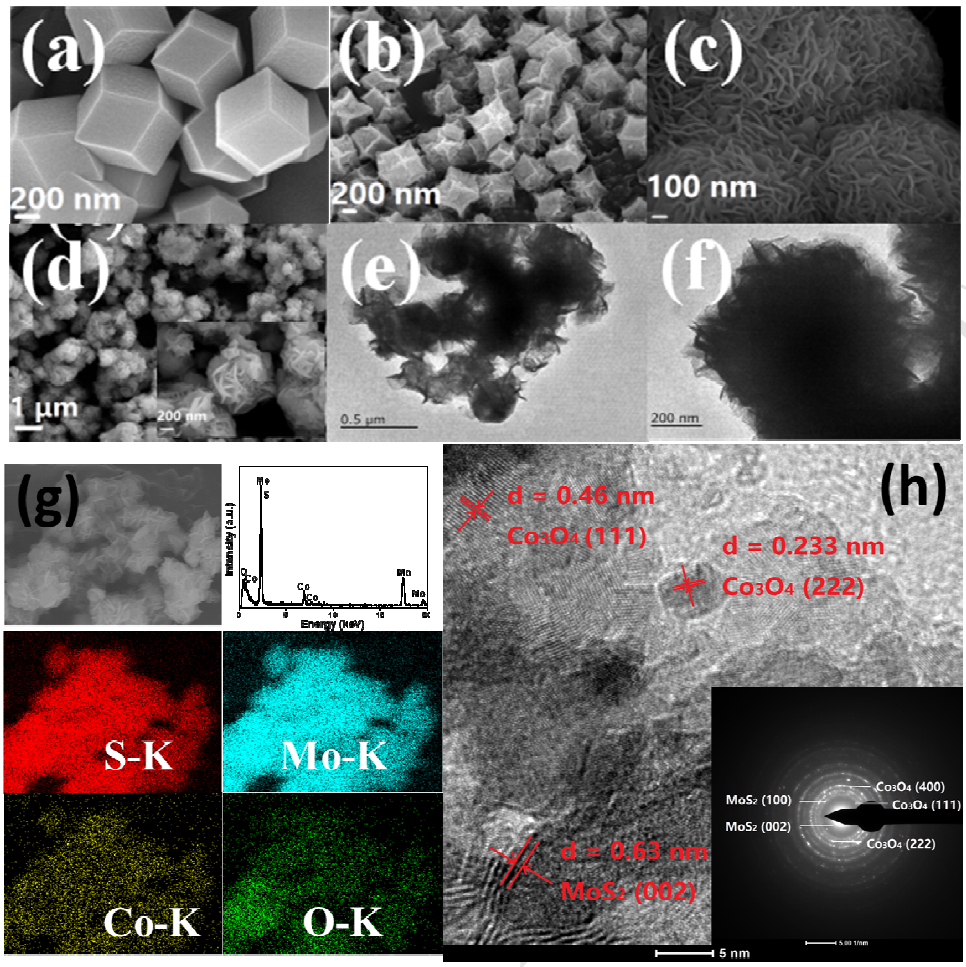

Fig. 3 SEM images of (a) ZIF-67, (b) Co_3O_4, (c) MoS_2, and (d) Co_3O_4/MoS_2 (inset: the image of Co_3O_4/MoS_2 at a high magnification). (e, f) TEM images of Co_3O_4/MoS_2 at different magnifications; (g) The EDS elemental mapping of S, Mo, Co and O; (h) HRTEM image of Co_3O_4/MoS_2 (inset: the corresponding SAED pattern).

3.4. Electrochemical performances

The Co_3O_4/MoS_2 composite has been used as an anode material for LIBs. Fig. 4a displays the first three CV cycles measured at a scan rate of 0.2 mV s^{-1} in the voltage range from 0.01 to 3.0 V. In the first cycle, the peak centered at 0.63 V can be resulted from the reduction of Co^{2+} (and Co^{3+}) to Co and the associated electrolyte decomposition accompanying with the formation of Li_2O [16, 38]. Meanwhile, a broad peak at 2.03 V in the charge process should be attributed to the decomposition of Li_2O and the oxidation of metallic Co into Co_3O_4 [30, 38]. These peaks are not found in the first three CV curves of bare MoS_2 (Fig. S3a). In the first discharge sweep, the peak exhibited at 1.11 V

could be ascribed to the intercalation of lithium ions into the hexagonal MoS_2 lattice accompanied by the phase transformation to octahedral Li_xMoS_2, according to the conversion reaction: $MoS_2 + xLi^+ + xe^{-1} \rightarrow Li_xMoS_2$ [40, 41]. Then, the broad and weak peak at 0.29 V is due to the decomposition of Li_xMoS_2 into Mo nanocrystals, which are embedded in a Li_2S matrix on the basis of the electrochemical reaction: $LixMoS_2 + (4 - x)Li^+ + (4 - x)e^{-1} \rightarrow Mo + 2Li_2S$ [45-48], and followed by the formation of a solid electrolyte interface (SEI) layer. After the first cycle, the reversible transformation reaction of sulfur to Li_2S, which is the main mechanism for lithium storage of MoS_2. Accordingly, the reduction peak at 2.32 V in the following cycles is account for the lithiation process of S to form Li_2S: $S + 2Li^+ + 2e^{-1} \rightarrow Li_2S$ [50, 51]. In the subsequent cycles, the oxidation-reduction peak become more stable, indicating that reversible electrochemical reactions of Co_3O_4/MoS_2 composite electrode are gradually created after the first cycle. However, the Co_3O_4 electrode (Fig. S3b) exhibits a decrease in the peak intensity from the 2nd cycle because of the incomplete de-conversion, serious agglomeration and huge structural reconstruction of metal oxides during cycling [42, 44, 49]. Fig. 4b depicts the charge/discharge voltage profiles of Co_3O_4/MoS_2 anode for the 1st, 2nd, and 100th cycles at a current density of 100 mA g^{-1} between 0.01 and 3.0 V. The composite electrode shows a high initial discharge capacity of 1136.4 mAh g^{-1}, a relative low charge capacity of 912.4 mAh g^{-1}, and the Coulombic efficiency (CE) of around 80.3%. The decomposition of electrolyte or some irreversible processes such as the formation of a solid-electrolyte interface layer during the first cycle can be the main reason for the low initial CE mainly [52]. Moreover, such a highly initial lithium storage capacity is likely to be in connection with the synergistic effect of Co_3O_4/MoS_2. From the 14th cycle, the electrochemical lithiation/delithiation process becomes very stable and the discharge capacity starts to increase to over 1000 mAh g^{-1}. The Co_3O_4/MoS_2 composite electrode can still remain a high capacity above 1000 mAh g^{-1} after 50 cycles (Fig. 4c), and reach to their maximum discharge capacity of ~1200 mAh g^{-1} after the first

100 cycles. However, pure Co_3O_4 and MoS_2 display the rapid and huge capacity decay during cycling (Fig. S4). Then, Co_3O_4/MoS_2 exhibits a coulombic efficiency of approximately over 97% from the 4^{th} cycle. These results demonstrate that the significantly improved electrochemical performance of Co_3O_4/MoS_2 electrode can be reasonably ascribed to the unique structure of Co_3O_4/MoS_2. On one hand, the inner Co_3O_4 particles stabilize the disordered structure of MoS_2, and suppress the volume expansion and shrinkage during the charge/discharge process, as well as avoid the loss of polysulfide intermediates. On the other hand, MoS_2 nanosheets covered on the surface of Co_3O_4 particles slow down the bulk change of Co_3O_4 during cycling [33-35]. For comparison, two Co_3O_4/MoS_2 samples with different mass ratios of MoS_2:Co_3O_4 are prepared by changing the mass (20 mg, 130 mg) of Co_3O_4 components during the synthesis process of composites. The as-obtained materials are named as L-Co_3O_4/MoS_2 and H-Co_3O_4/MoS_2, respectively. The morphologies and charge/discharge curves of both composites are shown in Fig. S5. Obviously, the specific capacities of these two composites decrease sharply with increasing the cycling numbers, which can be reasonably explained from their morphological features. For the H-Co_3O_4/MoS_2 sample, it can be found that some Co_3O_4 particles have not been covered by irregular MoS_2 nanosheets with various sizes. As a result, these exposed Co_3O_4 particles easily suffer from the pulverization during the charge/discharge reaction and then result in the fast decay of specific capacities for the composite electrode. For the L-Co_3O_4/MoS_2 sample, more sphere-like aggregated MoS_2 particles are formed, which offer much less active sites and also suffer from volume expansion during the cycling reaction, leading to the poor cycling stability for the composite electrode. So, we can conclude from above analysis that the moderate mass ratio of Co_3O_4:MoS_2 in the composite will facilitate the enhancement of electrochemical stabilities. The cycling performance of Co_3O_4/MoS_2 at 1 A g^{-1} is also carried out and shown in Fig. S6. The electrode still delivers a capacity of 275

mAh g^{-1} after 30 cycles and no obvious decay is observed, demonstrating a high specific capacity and cycling stability for such system even at higher current densities.

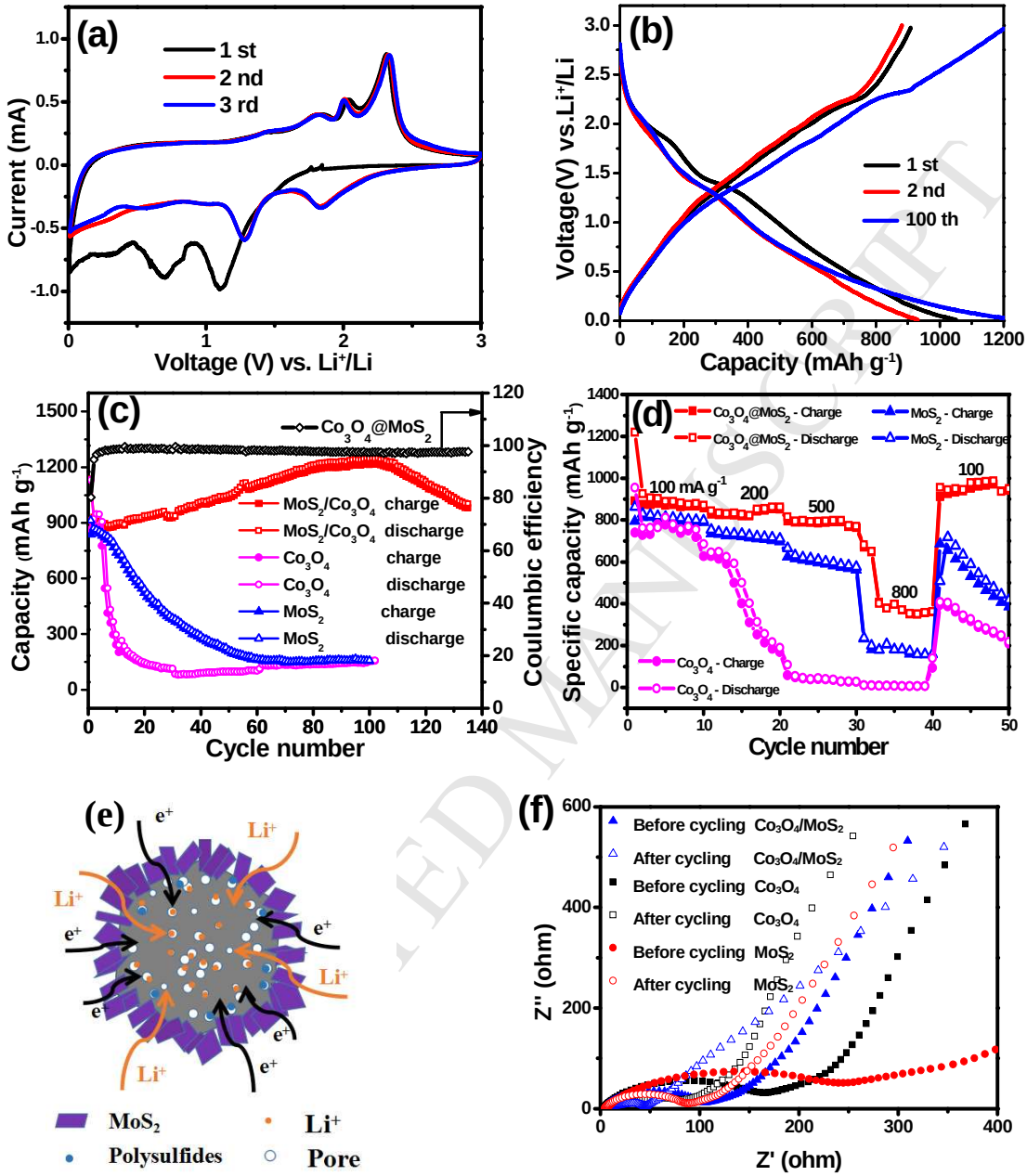

Fig. 4 (a) Cyclic voltammetry curves of Co_3O_4/MoS_2 measured at a scan rate of 0.2 mV s^{-1} in the voltage range of 0.01-3 V (vs. Li/Li^+); (b) Charge-discharge curves of Co_3O_4/MoS_2 at the current density of 100 mA g^{-1}; (c) Cycling performances for Co_3O_4, MoS_2 and Co_3O_4/MoS_2 at the current density of 100 mA g^{-1}; (d) Rate behavior of Co_3O_4, MoS_2 and Co_3O_4/MoS_2 at various current densities from 100 to 800 mA g^{-1}; (e) Electrochemical mechanism of Co_3O_4/MoS_2 consisting of electron transportation and ions diffusion; (f) Nyquist plots of Co_3O_4, MoS_2 and Co_3O_4/MoS_2 electrodes from

100 kHz to 0.01 Hz before and after 100 cycles at the current density of 100 mA g^{-1}.

The rate capabilities of Co_3O_4, MoS_2 and Co_3O_4/MoS_2 electrodes at various current densities are further investigated. Fig. 4d shows multiple-current galvanostatic measurements of Co_3O_4/MoS_2. Increasing the current densities gradually from 100 to 200, 500, and 800 mA g^{-1}, the capacities are 903.7, 833.1, 793.8, and 397.9 mAh g^{-1}, respectively. The capacities of the composite decrease slowly with increasing the current densities, manifesting a considerably better rate performance than pure Co_3O_4. In addition, upon the reversal of the current density from 800 to 100 mA g^{-1}, the specific capacity of the composite electrode is around 970 mAh g^{-1}.

This aforesaid result reveals that the good rate capability of the composite derived from the synergistic interaction between dodecahedra Co_3O_4 particles and MoS_2 nanosheets. At the same time, the curve of cycling performance presents that the capacities of the composite electrode increase gradually rather than decline during the first 100 cycles. It should be mentioned here that our composite has obvious advantages compared with other MoS_2 or Co_3O_4-based composite electrodes in the aspect of specific capacity (Table 1). Electrochemical mechanism of Co_3O_4/MoS_2 consisting of electron transportation and ions diffusion is shown in Fig. 4e [35]. Overall, the gradual permeation of electrolyte into the inner Co_3O_4 particles along with the activation of the outer MoS_2 nanosheets result in the increased reversible capacity during the first 100 cycles. Viewed from the structural perspective, the pores of Co_3O_4/MoS_2 mainly derive from porous Co_3O_4 dodecahedrons with tiny nanocrystallites and numerous MoS_2 nanosheets. This hierarchical porous structure not only enlarges the contact area of Co_3O_4/electrolyte, but also provides more spaces and electrochemically active surfaces for accommodating lithium ions. In addition, the outer MoS_2 nanosheets in the composite can offer more active sites for the insertion/extraction of lithium ions. Another fact is that the gradual formation of polymer/gel-like layer on the surface of electrode also facilitates the increasing of capacities [38]. However, the capacity begins to

decrease after 100 cycles, which may be attributed to the following facts. The redox reaction is usually accompanied by consuming part of the electrolyte during the charge/discharge process. Owing to the lack of electrolyte after cycling, the electrode can not be completely moist to the electrolyte. To further explore the reason of capacity decay, the morphologies of Co_3O_4/MoS_2 after cycling are performed and the SEM images are shown in Fig. S7. The pulverization of a small amount of particles is observed, although most of particles still maintain the integrity of structure and morphology. The combination of above factors results in the decrease of capacity after 100 cycles.

Table 1 Summary of capacitive performances of MoS_2 or Co_3O_4-based composite electrodes reported previously for LIBs

Materials	Specific Capacity ($mAh\ g^{-1}$)	Current ($mA\ g^{-1}$)	Cycle number (cycles)	Refs.
TiO_2-MoS_2	604	100	100	29
MoO_2/MoS_2	724	800	800	31
MoS_2/Co_3O_4	920	200	100	30
MNCD@MoS_2	~1230	100	120	35
TiO_2@MoS_2	971	100	200	40
Fe_2O_3/MoS_2	1350	100	150	41
Fe_3O_4/MoS_2	~700	2000	510	51
graphene/Co_3O_4	714	100	200	20
Co_3O_4(MOF-71)	913	200	60	52
Co_3O_4/CNT	880	50	100	21
Co_3O_4/TiO_2	642	500	200	19
Co_3O_4/MoS_2	1246	100	100	this work

Electrochemical impedance spectrometry (EIS) measurements were carried out before and after 100 cycles for the sake of further understanding the electrochemical performance of Co_3O_4, MoS_2 and Co_3O_4/MoS_2 electrodes. Nyquist plots (Fig. 4f)

show that the Co_3O_4/MoS_2 has the greatly smaller charge transfer resistance (Rct) than that of pure Co_3O_4 and MoS_2 before cycling between 100 kHz to 0.01 Hz. The impedance of Co_3O_4/MoS_2 and Co_3O_4, MoS_2 electrodes decreases significantly after the 100^{th} cycle, compared with the fresh cell. For the pure MoS_2 and Co_3O_4, the smaller charge transfer resistances after 100 cycles can be attributed to the more close contacts between particles and conductive agents after the pulverization occurred in the charge/discharge process. This result further confirms that the incorporation of MoS_2 nanosheets can greatly accelerate electron transmission during the lithiation/delithiation conversion, leading to the improved electrochemical performances [53, 54].

4. Conclusions

In summary, Co_3O_4 dodecahedrons with uniform morphology have been prepared through a direct pyrolysis of ZIF-67 and used as the substrates for the growth of MoS_2 nanosheets, resulting in the formation of Co_3O_4/MoS_2, where Co_3O_4 particles are uniformly covered by MoS_2 nanosheets. The resulting Co_3O_4/MoS_2 is applied as an anode material for LIBs. The ratio of Co_3O_4 and MoS_2 components in the composite is important for the enhancement of electrochemical performance. In the structure, the two-dimensional MoS_2 can not only provide a high specific capacity, but also prevent the particles aggregation and slow capacity attenuation. In addition, MoS_2 also releases the bulk volumetric change of Co_3O_4 during the charge and discharge process. In consequence, the composite delivers a high reversible capacity and cycling stability. It is believed that this facile synthetic strategy can be extend to other metal oxides/MoS_2 composites, and this type of materials can also be promising materials for other electrochemical applications such as supercapacitors, Na-ion storage and electrocatalysis.

Appendix A. Supporting information

Supplementary data associated with this article can be found in the online at http://dx.doi.org/....

Acknowledgements

This work was supported by the National Natural Science Foundation (51672114, 51272095), the Natural Science Foundation of Jiangsu Province

(Nos. BK20151328, BK20161357), the project of the Priority Academic Program Development of Jiangsu Higher Education Institutions.

References

[1] P. Simon, Y. Gogotsi, B. Dunn. Science 343 (2014) 1210-1211.

[2] H.J. Huang, J.X. Zhu, W.Y. Zhang, C.S. Tiwary, J.F. Zhang, X. Zhang, Q.G. Jiang, H.Y. He, Y.P. Wu, W. Huang, P.M. Ajayan, Q.Y. Yan. Chem. Mater 28 (2016) 1737-1745.

[3] D. Ji, H. Zhou, J. Zhang, Y.Y. Dan, H.X. Yang, A.H. Yuan. J. Mater. Chem. A 4 (2016) 8283-8290.

[4] H. Zhou, X.Q. Liu, J. Zhang, Y.J. Liu, A.H. Yuan. Int. J. Hydrogen Energy 39 (2014) 2160-2167.

[5] M.V. Reddy, G.V. Subba Rao, B.V. Chowdari. Chem. Rev. 113 (2013) 5364-5457.

[6] P.G. Bruce, B. Scrosati, J.-M. Tarascon. Angew. Chem., Int. Ed. 47 (2008) 2930-2946.

[7] Z.Q. Xie, W.W. Xu, X.D. Cui, Y. Wang. ChemSusChem. 10 (2017) 1645-1663.

[8] L. Wang, Y.Z. Han, X. Feng, J.W. Zhou, P.F. Qi, B. Wang. Coord. Chem. Rev. 307 (2016) 361-381.

[9] R.T. Wang, D.D. Jin, Y.B. Zhang, S.J. Wang, J.W. Lang, X.B. Yan, L. Zhan. J. Mater. Chem. A 5 (2017) 292-302.

[10] J. H. Zhang, M. Huang, B. J. Xi, K. Mi, A. H. Yuan, S. L. Xiong. Adv. Energy Mater. 8 (2018) 201701330.

[11] M. Huang, K. Mi, J.H. Zhang, H.L. Liu, T.T. Yu, A.H.Yuan, Q.H. Kong, S.L. Xiong. J. Mater. Chem. A 5 (2017) 266-274.

[12] Y. Wang, X.M. Guo, Z.K. Wang, Y. Wang, M.F. Lv, C. Yan, A.H. Yuan, H.X. Yang. J. Mater. Chem. A 5 (2017) 25562-25573.

[13] Y.Y. Chen, R. Cai, Y. Yang, C. Liu, A.H. Yuan, H.X. Yang, X.P. Shen, J. Alloys Compd. 698 (2017) 469-475.

[14] J.X. Guo, B. Jiang, X. Zhang, L. Tang, Y.H. Wen. J. Mater. Chem. A 3 (2015) 2251-2257.

[15] K.C. Klavetter, S. Garcia, N. Dahal, J. Snider, J. Pedrosouza, T. H. Cell, M.A. Cassara, A. Heller, S.M. Humphrey, C. B. Mullins. J. Mater. Chem. A 2 (2014) 14209-14221.

[16] L.M. Zhang, B. Yan, J.H. Zhang, Y.J. Liu, A.H. Yuan , G. Yang. Ceram. Int. 42 (2016), 5160-5170.

[17] T. Qi, S.C. Zhang, X.M. Wu, Y.L. Xing, G.R. Liu, Y.B. Ren. New J. Chem. 40 (2016) 3536-3542.

[18] Y.B. Lou, J. Liang, Y.L. Peng, J.X. Chen. Phys. Chem. Chem. Phys. 17 (2015), 8885-8893.

[19] W.W. Xu, X.D. Cui, Z.Q. Xie, G. Dietrich, Y. Wang. Electrochim. Acta. 222 (2016) 1021-1028.

[20] Q.T. Qu, T. Gao, H.Y. Zheng, X.X. Li, H.M. Liu, M. Shen, J. Shao, H.H. Zheng. Carbon, 92 (2015) 119-125.

[21] N.L. Venugopal, J. Yoo, W.S. Yoon. J. Nanosci. Nanotechno 17 (2017) 3390-3396.

[22] T. Stephenson, Z. Li, B. Olsen, D. Mitlin. Energy Environ. Sci. 7 (2014) 209-231.

[23] H.N. Li, Y.M. Shi, M.-H. Chiu, L.J. Li. Nano Energy 18 (2015) 293-305.

[24] X.D. Zhu, K.X. Wang, D.J. Yan, S.R. Le, R.J. Ma, K.N. Sun, Y.T. Liu. Chem. Commun. 51 (2015) 11888-11891.

[25] L.M. Xu, L. Ma, X.Y. Xu, X.P. Zhou, L.L. Zhang, W.X. Chen. Materials Letters, 173 (2016) 84-87.

[26] H.J. Kim, J.P. Cho. Nano Lett. 11 (2011) 4826-4830.

[27] C.Q. Feng, J. Ma, H. Li, R. Zeng, Z.P. Guo, H.K. Liu. Mater. Res. Bul. 44 (2009) 1811-1815.

[28] Y.L. Jia, H.Q. Wan, L. Chen, H.D. Zhou, J.M. Chen. J. Power Sources 354 (2017) 1-9.

[29] X.Q. Zhu, C. Yang, F. Xiao, J.D. Wang, X.T. Su. New J. Chem. 39 (2015)

683-688.

[30] Y.B. Lou, D. He, Z.F. Wang, Y.H. Hu, Y. Shen, J. Ming, J.X. Chen. Chem. Eng. J. 313 (2017) 1269-1277.

[31] Z.N. Deng, Y.J. Hu, D.Y. Ren, S.L. Lin, H. Jiang, C.Z. Li. Chem. Commun. 51 (2015) 13838-13841.

[32] T.R. Lin, J. Wang, L.Q. Guo, F.F. Fu. J. Phys. Chem. C 119 (2015) 13658-13664.

[33] Z.M. Wan, J. Shao, J.J. Yun, H.Y. Zheng, T. Gao, M. Shen, Q.T. Qu, H.H. Zheng. Small 10 (2014) 4975-4981.

[34] Y. Xia, B.B. Wang, X.J. Zhao, G. Wang, H. Wang. Electrochimi. Acta 187 (2015) 55-64.

[35] J. Shao, T. Gao, Q.T. Qu, Q. Shi, Z.C. Zuo, H.H. Zheng. J. Power Sources 324 (2016) 1-7.

[36] B. Ma, P.Y. Guan, Q.Y. Li, M. Zhang, S.Q. Zang. Acs App. Mater. Inter. 8 (2016) 26794-26800.

[37] T. Rui, S.J. Zhou, T.R. Ge, Z.M. Yuan, L.W. Yin. J. Mater. Chem. A 5 (2017) 4962-4971.

[38] J. Shao, Z.M. Wan, H.M. Liu, H.Y. Zheng, T. Gao, M. Shen, Q.T. Qu, H.H. Zheng. J. Mater. Chem. A 2 (2014) 12194-12200.

[39] R.B. Wu, X.K. Qian, X.H. Rui, H. Liu, B.L. Yadian, K. Zhou, J. Wei, Q.Y. Yan, X.Q. Feng, Y. Long, L.Y. Wang, Y.Z. Huang. Small 10 (2014) 1032-1038.

[40] B.J. Guo, K. Yu, H.Fu, Q.Q. Hua, R.J. Qi, H.L. Li, H.L. Song, S. Guo, Z.Q. Zhu. J. Mater. Chem. A 3 (2015) 6392-6401.

[41] B. Qu, Y. Sun, L.L. Liu, C.Y. Li, C.J. Yu, X.Y. Zhang, Y.J. Chen. Sci. Rep. 7 (2017) 42772.

[42] Y. Wang, C.Y. Wang, Y.J. Wang, H.K. Liu, Z.G. Huang. J. Mater. Chem. A 4 (2016) 5428-5435.

[43] K. Chang, W.X. Chen, L. Ma, H. Li, F.H. Huang, Z.D. Xu, Q.B. Zhang, J.Y. Lee. J. Mater. Chem. 21 (2011) 6251-6257.

[44] H.B. Geng, H.X. Ang, X.G. Ding, H.T. Tan, G.L. Guo, G.L. Qu, Y.G. Yang, J.W. Zheng, Q.Y. Yan, H.W. Gu. Nanoscale 8 (2016) 2967-2973.

[45] X.L. Wang, G. Li, M.H. Seo, F.M. Hassan, M.A. Hoque, Z.W. Chen. Adv. Energy Mater. 5 (2016) 1501106.

[46] M.J. Hwang, K.M. Kim, K.S. Ryu. J. Electroceram. 33 (2014) 239-245.

[47] C.Y. Zhao, J.H. Kong, X.Y. Yao, X.S. Tang, Y.L. Dong, S.L. Phua, X.H. Lu. ACS Appl. Mater. Inter. 6 (2014) 6392-6398.

[48] J. Wang, J.L. Liu, D.L. Chao, J.X. Yan, J.Y. Lin, Z.X. Shen. Adv. Mater. 26 (2014) 7162-7169.

[49] D. Ji， H. Zhou, Y.L. Tong, J.P. Wang, M.Z. Zhu, T.H. Chen, A.H. Yuan. Chem. Eng. J. 313 (2017) 1623-1632.

[50] K. Chang, W.X. Chen. ACS Nano. 5 (2011) 4720-4728.

[51] Y. Chen, B.H. Song, X.S. Tang, L. Lu, J.M. Xue. Small 10 (2014) 1536-1543.

[52] C. Li, T.Q. Chen, W.J. Xu, X.B. Lou, L.K. Pan, Q. Chen , B.W. Hu. J. Mater. Chem. A 3 (2015) 5585-5591.

[53] S.J. Ding, D.Y. Zhang, J.S. Chen, X.W. (David) Lou. Nanoscale 4 (2012) 95-98.

[54] X. Xu, Z.Y. Fan, X.Y. Yu, S.J. Ding, D.M. Yu, X.W. (David) Lou. Adv. Energy Mater. 4 (2015) 1-5.

- The unique MOF-derived Co_3O_4 covered by MoS_2 nanosheets was prepared by a facile method.
- MOF-derived metal oxides/MoS_2 composites were used as electrode materials for the first time.
- The composite electrode showed excellent electrochemical properties for LiBs.